ADVANCED FUNCTIONAL MATERIALS
www.afm-journal.de

Inverse Solvation Configuration Induced by Organic Small-Molecule Spatially-Confined Coordination Enables Highly Reversible Zinc Batteries

Tiantian Lu, Shi Wang, Chang Liu, Lifeng Hou, Yinghui Wei, Qian Wang, and Zhong Jin**

Despite the cost and safety advantages of zinc-ion batteries (ZIBs), they still suffer from poor reversibility of Zn anodes in aqueous electrolytes, particularly under harsh conditions such as extreme temperatures and high depth of discharge. Herein, a low-concentration small-molecule spatially confined coordination electrolyte (0.45 M $Zn(BF_4)_2 \cdot xH_2O$–THF) is developed that reconstructs the Zn^{2+} solvation structure, forming a unique "inverse solvation configuration" rich in organic small molecules, thereby accelerating the de-solvation process of Zn^{2+} and forming a favorable and thin (≈50 nm) organic–inorganic hybrid SEI layer to achieve high interfacial stability. Concurrently, tetrahydrofuran can alter the inherent hydrogen bonding network and reduce the freezing point, ensuring stable solvation structure under harsh low-temperature conditions. As a result, the Zn || Zn symmetrical cells can be cycled for over 7000 h at low temperature, and the Zn || PANI full cells demonstrate impressive cycling stability over 18 000 cycles (−40 °C) with a capacity retention rate ≈100%. Importantly, even at a high discharge depth of 60%, Zn || Zn symmetrical cells can still maintain stable plating/stripping behavior over 3500 h. This work provides new insights for the electrolyte design of high-performance ZIBs.

1. Introduction

Lithium ion batteries (LIBs) have been widely used in portable electronic devices and electric vehicles due to their high energy density and long cycle life.[1–5] However, their further application is severely limited by limited Li resources in the crust and high cost.[6–8] Among the various next-generation energy storage battery systems, ZIBs are considered the most promising energy storage solution, owing to the high theoretical capacity (820 mAh g^{-1}), low redox potential (−0.762 V vs standard hydrogen electrode), and high abundance of Zn metal anode.[9,10] Unfortunately, in conventional aqueous electrolytes, the H_2O molecules within the Zn^{2+} solvation sheath $[Zn(H_2O)_6{}^{2+}]$ exhibit high chemical reactivity, leading to inevitable challenges at the zinc anode, such as: hydrogen evolution reaction (HER), surface corrosion, and dendritic Zn growth, which seriously hinders its reversibility and cycling life.[11–13] Besides, the large-scale commercial application of ZIBs is also severely obstructed by harsh service conditions, e.g., low temperature, ultra-long cycling and high discharge depth. Specifically, in low-temperature environments (−20 °C even −40 °C), aqueous electrolytes will freeze into a solid state, causing the reaction kinetics to become extremely slow, thus preventing ZIBs from working properly.[14–16] Furthermore, the Zn plating/stripping behavior is extremely uneven at high discharge depths, lowering the interface stability of Zn metal anode.[17] Therefore, it is necessary to develop advanced electrolyte systems to improve the interface stability of Zn metal anode and ensure the ZIBs can run stably in harsh conditions.

During the past decade, many electrolyte design strategies have been proposed to address the above-mentioned issues, achieving high-performance ZIBs. Typical strategies include: using high concentration electrolytes; adding electrolyte additives; constructing deep eutectic electrolytes; Co-solvent Strategy.[18–24] Among them, high concentration electrolytes can lower the solidification point of aqueous electrolyte and regulate the Zn^{2+} solvation structure, as well as reduce the reactivity of active water molecules, which are considered a simple and effective strategy to achieve high-performance ZIBs in harsh environments. For example, Zhang et al. reported a 7.5 M $ZnCl_2/H_2O$ electrolyte,

T. Lu, C. Liu, L. Hou, Y. Wei, Q. Wang
College of Materials Science and Engineering
Taiyuan University of Technology
Taiyuan, Shanxi 030024, China
E-mail: qianwang0825@pku.edu.cn

S. Wang
State Key Laboratory of Organic Electronics and Information Displays (SKLOEID), Institute of Advanced Materials (IAM)
Nanjing University of Posts & Telecommunications
Nanjing 210023, China

Z. Jin
State Key Laboratory of Coordination Chemistry, MOE Key Laboratory of Mesoscopic Chemistry, MOE Key Laboratory of High Performance Polymer Materials and Technology, Jiangsu Key Laboratory of Clean Energy Catalysis and Intelligent Green Chemical Engineering, Suzhou Key Laboratory of Green Intelligent Manufacturing of New Energy Materials and Devices, Tianchang New Materials and Energy Technologies Research Center, Institute of Green Chemistry and Engineering, School of Chemistry and Chemical Engineering
Nanjing University
Nanjing 210023, China
E-mail: zhongjin@nju.edu.cn

The ORCID identification number(s) for the author(s) of this article can be found under https://doi.org/10.1002/adfm.202523416

DOI: 10.1002/adfm.202523416

in which the freezing point of electrolyte was decreased to −114 °C due to the disruption of the original hydrogen bonding network in $ZnCl_2$-based electrolyte.[25] However, the high cost, high viscosity, and poor ion conductivity of high-concentration electrolytes constrain their further development. More importantly, some high-concentration electrolyte systems may experience Zn salt precipitation at low temperatures. By comparison, adding electrolyte additives is the most common strategy due to its simple operation and strong compatibility, such as: dimethyl sulfoxide, acetamide, and propan-2-ol, etc.[26–28] Thanks to the high polarity of organic molecules(OM), the Zn^{2+} solvation structure is reshaped, forming a solvation structure coordinated by trace amounts of organic molecules $[Zn(H_2O)_5(OM)^{2+}]$, thereby improving the electrochemical performance of ZIBs. However, due to the continuous consumption of additives during the charging and discharging cycle, the composition of SEI film on Zn electrode surface is uncontrollable, and it is prone to rupture during the cycling process, making it unable to adapt to the volume changes of Zn metal anode, resulting in uneven Zn deposition behavior and serious side reactions, especially in high discharge depth. Besides, most additives have a relatively single function and cannot meet the challenges of ZIBs in different application environments. Recently, eutectic electrolytes and co-solvent electrolytes have garnered significant attention due to their stable and ordered solvation structures. Typically, Lin et al. reported a novel eutectic electrolyte composed of $Zn(ClO_4)_2{\cdot}6H_2O$ and sulfolane, in which Zn || PANI full cells can be cycled >500 cycles at −20 °C.[29] The strong coordination between sulfolane and Zn^{2+} triggered a deep eutectic effect, forming unique solvation structure, thus promoting uniform Zn deposition and reducing water reactivity. However, up to now, the electrochemical performance of eutectic electrolytes in harsh environments is still poor, such as: low coulombic efficiency (CE), poor lifespan under high discharge depth. This is mainly because traditional eutectic electrolytes cannot effectively lock in active water and form stable SEI film to promote Zn^{2+} diffusion. Li et al. reported a mixed-phase ethyl acetate (EA)/water co-solvent electrolyte system to alter the solvation structure of Zn^{2+} and disrupt the original strong hydrogen bond network formed by H_2O, thereby enabling 600 cycles at −40 °C in Zn||Active Carbon zinc-ion capacitors.[30] However, co-solvents employed in this strategy often exhibit high viscosity, potentially reducing ionic conductivity. Simultaneously, co-solvent molecules may preferentially adsorb at the electrode interface or undergo decomposition, introducing new interfacial reactions. More importantly, eutectic electrolytes and co-solvent electrolytes usually have high concentrations, which goes against the original intention of developing low-cost ZIBs. Therefore, there is an urgent need to develop low-cost and simple yet efficient electrolyte systems to achieve stable run of ZIBs in harsh conditions, which remains a serious challenge.

Here, we have developed an extremely simple low-concentration (0.45 M) small-molecule spatially confined coordination electrolyte composed of zinc tetrafluoroborate ($Zn(BF_4)_2{\cdot}4.6H_2O$) and tetrahydrofuran (THF). Benefiting from the weak polarity, low viscosity, and low freezing point of THF, the 0.45 M borate-furan electrolyte displayed a high ionic conductivity of 21.5 mS cm^{-1}.

More importantly, THF molecules dominate the primary solvation sheath of Zn^{2+}, effectively excluding water molecules to the outer secondary solvation shell or even into a free state. This spatial confinement effect promotes the formation of a unique inverse solvation configuration, $[Zn(THF)_3(H_2O)]^{2+}{\cdot}(BF_4^-)_2$, which drastically reduces the number of reactive water molecules in direct contact with the zinc anode. This structure fundamentally reverses the conventional solvation paradigm dominated by the highly aqueous $[Zn(H_2O)_6]^{2+}$ complex, thereby effectively suppressing corrosion and hydrogen evolution reactions and ensuring highly stable operation of zinc-ion batteries under harsh conditions. In addition, FIB-TEM and TOF-SIMS showed that a highly hybrid organic–inorganic SEI layer with ≈50 nm thick can form in this inverse solvation configuration electrolyte, regulating the Zn^{2+} diffusion and migration, thus enhancing the reversibility of Zn plating/stripping process and achieving dendrite-free and dense Zn deposition behavior (**Figure** 1a). By that, using thin Zn foils (30 µm) as electrodes, the ZIBs exhibited a comprehensive improvement in electrochemical performance, especially under low temperature (−20 and −40 °C) and high discharge depth. Zn || Zn symmetric cells showed ultralong cycling for >7000 h at the current density of 0.5 mA cm^{-2} at −20 °C, while Zn || PANI full cells did not show significant capacity degradation even after 18 000 cycles at the current density of 0.5 A g^{-1} at −40 °C. More attractive thing is that even at a high discharge depth of 60%, the cells can achieve stable Zn plating/stripping behavior over 3500 h at −20 °C, manifesting one of the best results in Zn metal anodes. This work opens the door to a new world for improving the stability of Zn metal anode in harsh environments and promoting the practical application of ZIBs in large-scale energy storage system.

2. Result and Discussion

2.1. Design Concept and Solvation Structure in Borate-Furan Electrolyte

Zinc tetrafluoroborate, which is cheaper than the commonly used Zn salts in ZIBs, such as: $ZnSO_4$, $Zn(OTF)_2$, $Zn(ClO_4)_2$, etc, making it one of the most ideal choices for promoting the commercialization of ZIBs (Figure S1, Supporting Information). Meanwhile, it can help to form a ZnF_2-riched SEI film on the Zn anode surface during charging and discharging cycles, improving interface stability. However, zinc tetrafluoroborate comes with crystalline water at the beginning of its preparation. Thermogravimetric analysis (TGA) suggested that 1.0 M the purchased zinc tetrafluoroborate contains 4.6 M H_2O, that is: $Zn(BF_4)_2{\cdot}4.6H_2O$ (Figure S2, Supporting Information). To determine the specific moisture content in the electrolyte, KF titration experiments were conducted. After multiple measurements, the water content of the ZFT electrolyte was found to be ≈4.71% (Figure S3, Supporting Information). When it is directly applied to aqueous electrolytes, due to the strong hydrolysis of BF_4^- ions, electrolyte will exhibit strong acidity (≈0.7 pH), leading to severe corrosion and hydrogen evolution reactions, which markedly constrain its practicality (Figure 1b).[31] Choosing appropriate organic solvents instead of H_2O is the most direct strategy to solve the aforementioned problems. Currently common organic solvents, such as dimethyl sulfoxide (DMSO), trimethyl phosphate (TMP) and dimethyl carbonate (DMC) have a large molecular structure, which will form aggregates with large radius during the

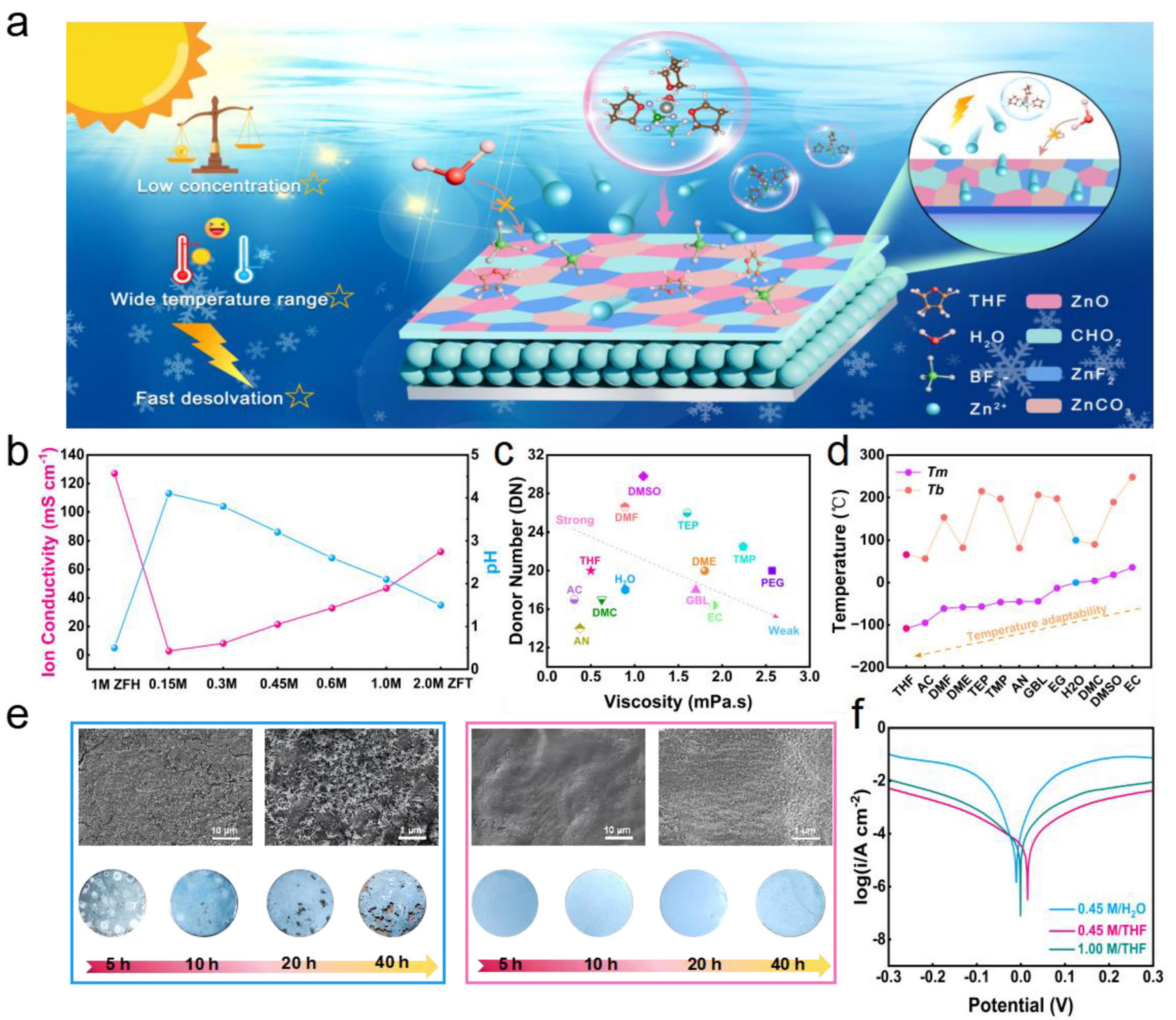

Figure 1. Design concept and main mechanism of electrolyte. a) Design concept of electrolyte; b) Ion conductivity and pH of different electrolytes at room temperature; c) Donor number and viscosity of common solvents; d) Temperature adaptability of common solvents; e) SEM images and digital photos of Zn soaked in ZFH (Left) and ZFT (Right); f) Tafel curves of Zn || Zn symmetrical cells in Different electrolytes.

solvation process.[32–34] The large molecular configuration hinders the de-solvation process of Zn^{2+} ions, which restricts their use under harsh conditions, such as: poor low-temperature performance (low ion conductivity and Zn salt precipitation at low temperature), hardly meeting the actual needs of high-performance ZIBs. In addition, some typical organic electrolytes have increased costs due to the high concentration of Zn salts (>3.0 M), which goes against the original intention of ZIBs.[35] Here we start from the design process of the electrolyte and choose tetrahydrofuran (THF) as the solvent for dissolving $Zn(BF_4)_2$ due to its high donor number, low viscosity, and low freezing point, achieving an extremely simple $Zn(BF_4)_2$/THF electrolyte to ensure the stable run of ZIBs under harsh conditions (Figure 1c,d). Subsequently, we first investigated the self-corrosion behavior of Zn metal in electrolyte. As shown in Figure 1e, when Zn foil was immersed in the $Zn(BF_4)_2/H_2O$ electrolyte (defined as: ZFH electrolyte), after only 5.0 h, its surface lost metallic luster and formed a passivation layer. Extending the immersion to 40 h, Zn foil surface exhibited severe corrosion and needle-like corrosion morphology, suggesting that Zn foil was extremely thermodynamically unstable in ZFH electrolyte with strong acidity. On the contrary, there were no obvious side reactions on the Zn foil surface when Zn foil was immersed in the $Zn(BF_4)_2$/THF electrolyte (defined as: ZFT electrolyte) for >40 h, the corresponding EDS spectrum also indicated that HF generated from the decomposition of BF_4^1 anions in water caused corrosion of the zinc electrode. The fluorine content on the surface of zinc foil immersed in ZFH electrolyte (2.55%) was significantly higher than that in ZFT electrolyte (0.29%) (Figure S4, Supporting Information). Meanwhile, XRD patterns demonstrated that there were a large number of corrosion products on Zn foil surface after soaking in the ZFH electrolyte, whereas no discernible by-products were detected when soaking in the ZFT electrolyte, suggesting that self-corrosion was significantly inhibited (Figure S5, Supporting Information).

Furthermore, we investigated the effect of ZFT electrolyte concentration. As shown in Figure 1b, the ion conductivity of 1.0 M $Zn(BF_4)_2$/THF electrolyte was as high as 46.8 mS cm^{-1}, and even the concentration decreased to 0.45 M, owing to the strong coordination ability of THF, the electrolyte still displayed a high ion conductivity of 21.5 mS cm^{-1}, which was sufficient to support the stable run of ZIBs. Meantime, compared with $Zn(BF_4)_2/H_2O$ electrolyte and 1.0 M $Zn(BF_4)_2$/THF electrolyte, 0.45 M $Zn(BF_4)_2$/THF electrolyte exhibited a more positive corrosion potential, helping to suppress the electrochemical decomposition of H_2O, this may be due to the presence of more reactive water molecules in 1.0 M $Zn(BF_4)_2$/THF, which are more likely to participate in the solvation structure of Zn^{2+} and corrode the Zn electrode during the de-solvation process (Figure 1f). Therefore, 0.45 M $Zn(BF_4)_2$/THF electrolyte was adopted as the optimized concentration. After preparing the 0.45 M $Zn(BF_4)_2$/THF (ZFT) electrolyte, the solvation structure was characterized. As shown in **Figure 2a**, the FTIR spectrum showed that there was a strong hydrogen bond (≈3200 cm^{-1}) in the $Zn(BF_4)_2/H_2O$ (ZFH) electrolyte, while the strong hydrogen bonding was not detected in the ZFT electrolyte, indicating a significant decrease of water activity in the electrolyte, which was beneficial for suppressing the side reactions on the Zn anode surface.[33,36] Compared with ZFH electrolyte, the results of Raman spectroscopy showed that BF_4^- changed from free state to bound state, which made it easier to combine with Zn^{2+}. Meanwhile, the introduction of the $Zn(BF_4)_2$ salt caused the Raman characteristic peak of pure THF C—O bond to shift toward higher wavenumbers, indicating that an interaction occurred between THF and Zn^{2+}. The shift of the $-CH_2$ characteristic peak in the 2850–3000 cm^{-1} range also confirmed this result (Figure S6, Supporting Information). Further, in the corresponding ^{1}H NMR spectrum, the characteristic peak of $-CH_2$ exhibited a shift toward lower fields, which was primarily due to the coordination between Zn^{2+} and THF leading to a decrease in the electron density of the O atom in C–O–C. This effect was transmitted to the adjacent $-CH_2$ through the inductive effect, resulting in a shielding effect. This also indirectly confirmed that THF entered the solvation structure of Zn^{2+} (Figure S7, Supporting Information). Furthermore, compared with ZFH electrolyte, the ^{19}F peak in the NMR spectra was shifted to a higher field, suggesting that the competitive coordination of THF can make it easier for FBF_3^- to detach from the solvation sheath, leading to an increase in the electron density, thereby contributing to the formation of ZnF_2-rich SEI (Figure 2b). Theoretically, density functional theory (DFT) calculations showed that the binding energy order between different components in the electrolyte was Zn^{2+}-BF_4^- > Zn^{2+}-THF> Zn^{2+}-H_2O, indicating that Zn^{2+} can preferentially coordinate with THF rather than H_2O molecules, effectively breaking the hydrogen bonding network of H_2O molecules in the electrolyte and changing the Zn^{2+} coordination environment (Figure 2c). The calculation results of adsorption energy demonstrated that THF was more easily adsorbed on the Zn surface than H_2O molecules, constructing a stable metal-molecule interface protective layer and reducing side reactions (Figure S8, Supporting Information). Molecular dynamics (MD) simulation was also conducted to identify the solvation structure. As shown in Figure S9 (Supporting Information), in the ZFH electrolyte, BF_4^- hardly participated in the Zn^{2+} coordination, indicating that the solvation structure of the ZFH electrolyte was a typical $[Zn(H_2O)_6]^{2+}$ structure. This solvation structure, dominated by low entropy solvent separated ion pairs (SIP), has a high symmetry and more energy is required to disrupt this highly ordered structure during the de-solvation process. However, for ZFT electrolyte, it can be seen that BF_4^-, THF molecules and H_2O molecules jointly participate in the solvation sheath of Zn^{2+}, forming a disordered solvation structure, and the radial distribution function (RDF) confirmed that the coordination distances of these components were ≈0.2 nm and the average coordination numbers were 2.50, 3.18, 0.32, respectively, which was consistent with the above results (Figure 2d,e).[37] Furthermore, Gibbs free energy calculations demonstrated that $[Zn(THF)_3(H_2O)]^{2+}\cdot(BF_4^-)_2$ has the lowest Gibbs free energy and the most stable structure. Thus, $[Zn(THF)_3(H_2O)]^{2+}\cdot(BF_4^-)_2$ was identified as the predominant solvation structure (Figure 2f; Figure S10, Supporting Information). At the same time, the electrostatic potential of $[Zn(THF)_3(H_2O)]^{2+}\cdot(BF_4^-)_2$ was smaller than that of $[Zn(H_2O)_6]^{2+}$, indicating that THF can reduce the electrostatic repulsion between Zn^{2+} ions, thereby enhancing the Zn^{2+} diffusion and migration (Figure 2g). Besides, the HOMO energy level of THF molecules was higher (−6.82 eV) than that of H_2O molecules (−8.79 eV), while the LUMO energy level of THF molecules decreased from 0.11 eV (free state) to −0.83 eV (bound state), indicating that the bound state THF was easier to detach from the solvation sheath, which was conducive to the formation of stable SEI layer on Zn surface during charging and discharging process (Figure 2h). This unique configuration originated from the strong coordination capability of THF in a solvent-rich environment, where THF molecules dominated the primary solvation sheath of Zn^{2+} and effectively excluding water molecules to the outer secondary solvation shell or even into a free state. This spatial confinement effect promoted the formation of a unique inverse solvation configuration fundamentally distinct from the traditional water-dominated solvation shell structure ($[Zn(H_2O)_6]^{2+}$) (Figure S11, Supporting Information). Therefore, the reduction of active water in the inverse solvation configuration can increase the hydrogen precipitation overpotential and achieve a larger electrochemical window than in the aqueous-phase electrolyte (Figure 2i,j). Further, the de-solvation ability of different electrolytes was evaluated (Figure 2k; Figure S12, Supporting Information). Compared with ZFH (E_a = 41.42 kJ mol^{-1}), ZFT displayed a smaller de-solvation energy (E_a = 26.94 kJ mol^{-1}), indicating that the disordered "inverse solvation configuration" in ZFT can accelerate the de-solvation process. To sum up, THF can preferentially coordinate with Zn^{2+} and spatially confines reactive water molecules away from the solvation shell. This mechanism fundamentally alters the Zn^{2+} coordination environment, forming a special inverse solvation configuration enriched with organic small molecules and promoting the dissociation of solvation clusters and improving the reduction stability of the electrolyte, and protect the zinc anode from the effects of side reactions, such as hydrogen evolution and corrosion.

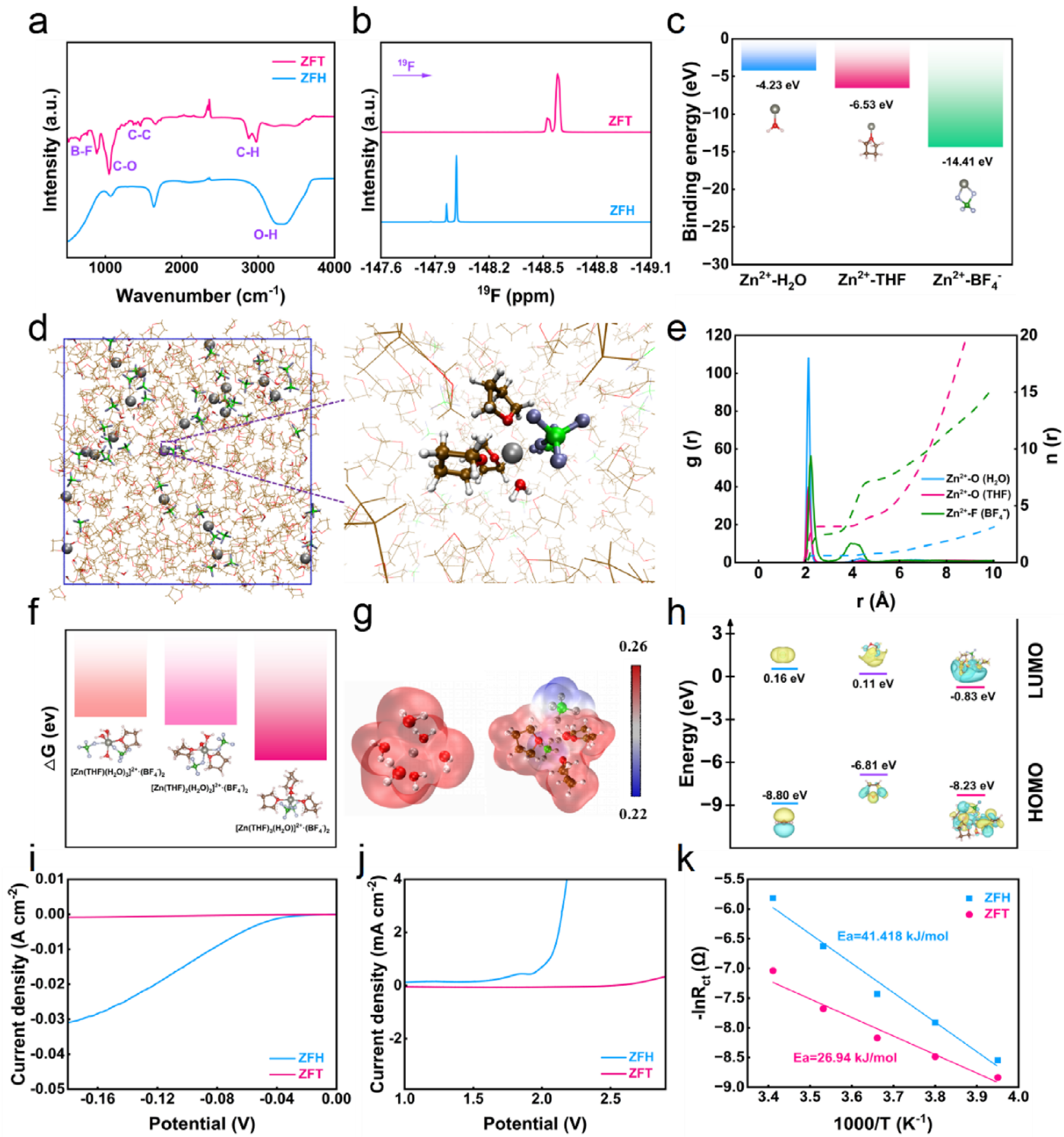

Figure 2. Solvation structure in borate-furan electrolyte. a) FTIR spectra and b) ^{19}F NMR spectra of ZFH and ZFT electrolytes; c) Binding energies of Zn^{2+}–H_2O, Zn^{2+}–THF and Zn^{2+}–BF_4^- and the corresponding model; d) 3D snapshots of ZFT obtained from MD simulations and partially enlarged snapshots of the solvation structure of Zn^{2+}; e) RDF plots for Zn^{2+}-O (H_2O), Zn^{2+}-O (THF), and Zn^{2+}-F (BF_4^-) pairs, and corresponding coordination numbers in ZFT; f) Gibbs free energy comparison of possible structures in ZFT; g) The electrostatic potential of $[Zn(H_2O)_6]^{2+}$ and $[Zn(THF)_3(H_2O)]^{2+}\cdot(BF_4^-)_2$; h) HOMO/LUMO energy levels of H_2O/THF/$[Zn(THF)_3(H_2O)]^{2+}\cdot(BF_4^-)_2$; i) LSV curves of Zn electrode in different electrolytes; j) Electrochemical stability windows in ZFH/ZFT; k) Arrhenius curves and activation energies of Zn2+ deposition on Zn anode in ZFH and ZFT.

2.2. Formation and Characterization of SEI Film in Borate–Furan Electrolyte

To accurately reveal the effect of ZFT electrolyte on SEI formation, Zn electrode surface after cycling was analyzed in detail. As shown in **Figures** 3a and S13 (Supporting Information), after cycling 50 cycles at the current density of 1.0 mA cm^{-2}, the cross-sectional analysis exhibited that the SEI layer induced by the “inverse solvation configuration” was clearly visible and relatively uniform, with a thickness of ≈50 nm. The EDS mapping showed that the SEI layer was mainly composed of C, O, Zn, and F elements and the surface distribution was relatively uniform,

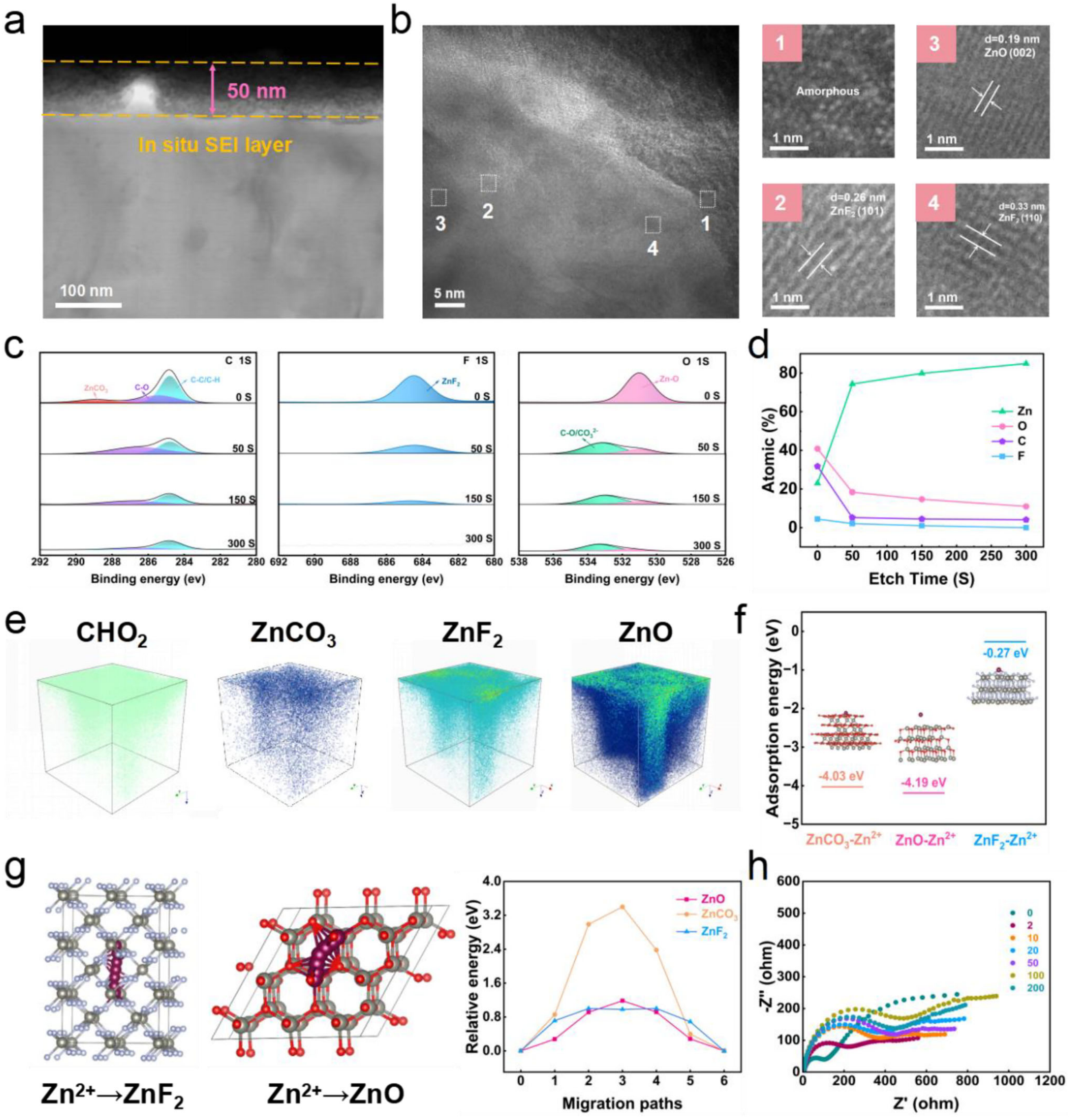

Figure 3. Formation and characterization of SEI film in borate–furan electrolyte. a) FIB-TEM cross-sectional images of the Zn electrode cycled in the ZFT electrolyte; b) HRTEM images of the Zn electrodes cycled in the ZFT electrolyte; c) C 1s, F 1s and O 1s XPS spectra with various Ar sputtering times; d) Atomic composition ratios of the SEI on the cycled Zn electrode at different Ar sputtering times; e) The corresponding 3D image reconstruction of ion spatial distributions from TOF-SIMS depth profiles; f) Adsorption energy of Zn^{2+} with $ZnCO_3$, ZnO and ZnF_2; g) The migration pathways and corresponding migration energy barriers of Zn^{2+} in ZnO and ZnF_2; h) EIS measurements after different number of cycles.

which may correspond to ZnF_2, ZnO, and some organic hybrids. Furthermore, HRTEM images confirmed the presence of lattice fringes of ZnF_2 and ZnO, as well as the presence of amorphous phases, indicating the formation of organic–inorganic hybrid SEI layer derived from unique solvation structures (Figure 3b).

XPS with various sputtering times was also used to analyze the SEI components and their depth distribution. As shown in Figure 3c, the C 1s spectra confirmed the presence of carbon-rich organic layer, such as: C—H/C—C, C—O, C═O, which can be attributed to the incomplete reduction products of THF. And the presence of ZnF_2 and ZnO can be confirmed by the O 1s and F 1s spectra.[38] As the etching depth increasing, the characteristic peak of F 1s, O 1s, and C 1s weakened, indicating the formation of highly hybrid organic–inorganic SEI layer (Figure 3d). TOF-SIMS depth profiling was performed to further analyze the composition distribution of SEI, and Figure 3e showed the 3D distribution of several ion mode fragments (-CHO_2, -$ZnCO_3$, -ZnF_2, and -ZnO) of the Zn surface depth profile after 50 cycles in ZFT electrolyte. The uniform distribution of C/O-containing inorganic and organic compounds on the Zn surface and in the deeper layers indicated the uniformity and density of SEI. The results were also consistent with TEM and XPS characterizations. Furthermore, the roles of various components in the SEI during Zn deposition process were analyzed. In inorganic components, compared with zinc carbonate and zinc fluoride, zinc oxide had a higher affinity for zinc ions and a smaller migration energy barrier (Figure 3f,g; Figure S14, Supporting Information). This means that during the de-solvation process, zinc oxide in the SEI can serve as the main channel for Zn^{2+} migration and deposition, promoting the Zn^{2+} transport and regulating the Zn^{2+} deposition behavior. Meanwhile, ZnF_2 functions as a dense physical barrier, helping to homogenize the Zn^{2+} flux and effectively suppress the initiation and growth of Zn dendrites. Therefore, the synergy between ZnO and ZnF_2 achieves an optimal balance of rigidity and flexibility: the rigid ZnF_2 layer provides structural stability and chemical passivation, while the flexible and ion-conductive ZnO layer facilitates efficient ion transport and stress dissipation. This complementary mechanism is crucial for ensuring a stable electrode-electrolyte interface and outstanding long-term cycling performance. Furthermore, the presence of organic components further enhances the stability of the SEI, as shown in Figure 3h, the EIS of symmetric cells showed a slight increase in the initial 10 cycles, corresponding to the formation of SEI film. Subsequently, even after 200 cycles, the impedance remained almost unchanged, suggesting that the SEI layer derived from the inverse solvation configuration of $[Zn(THF)_3(H_2O)]^{2+}\cdot(BF_4^-)_2$ had high stability, which endowed the long cycle stability of Zn metal anode. In short, such a SEI film can help stabilize the interface chemical environment and regulate the Zn^{2+} deposition behavior, thereby greatly improving the cycling stability of ZIBs.

2.3. Nucleation and Growth Behavior of Zn^{2+} in Borate-Furan Electrolyte

To investigate the impact of borate-furan electrolyte on Zn^{2+} nucleation and deposition behavior, the initial nucleation overpotential during the Zn deposition process was investigated. As shown in **Figure 4a**, at a polarization voltage of −150 mV, the response current in the $Zn(BF_4)_2/H_2O$ electrolyte continued to increase, indicating an increase in the contact area between Zn metal anode and the electrolyte, thereby resulting in forming more electrodeposition sites, eventually increasing the Zn deposition rate and forming irregular 3D structure, known as the infamous “tip effect”. In contrast, for the ZFT electrolyte system, the response current only slightly increased in the initial stage and then remained constant, which revealed that the random 2D Zn^{2+} diffusion on the electrode surface was limited, resulting in continuous 3D diffusion, thereby achieving the lateral and parallel Zn deposition.[39] Similarly, cyclic voltammetry (CV) curves were also used to investigate the Zn^{2+} nucleation behavior, which was shown in Figure 4b. Compared with the $Zn(BF_4)_2/H_2O$ electrolyte system, the nucleation overpotential in the ZFT electrolyte system increased by ≈56 mV, which can help to form smaller Zn nuclei.[40] Furthermore, ZFT electrolyte demonstrated better Zn metal wettability, exhibiting a small contact angle (≈4.9°) on the Zn surface, thus ensuring Zn^{2+} uniform flow and fast Zn^{2+} transport kinetics (Figure S15, Supporting Information).

The SEM and TEM images were used to characterize the deposition and growth behavior of Zn. As shown in Figure 4c and Figure S16 (Supporting Information), the Zn deposition in ZFH exhibited sharp and loose needle-like morphology, which was attributed to parasitic reactions and uneven Zn nucleation behavior. In contrast, the ZFT electrolyte exhibited a more uniform Zn deposition behavior, resulting in a clear crystal structure and highly dense morphology. From the TEM results, it can be seen that the Zn deposition layer in the ZFH electrolyte demonstrated a large amount of disordered amorphous structure, which can be attributed to the by-products of hydrogen evolution and corrosion reactions, while in the ZFT electrolyte system, there were significant hexagonal aggregates, which conformed to the ideal Zn crystal structure (Figure 4d; Figure S17, Supporting Information). In order to observe the Zn deposition behavior more intuitively, an in situ optical device was carried out to observe the real-time Zn deposition morphology. As shown in Figure 4e, at a current density of 10 mA cm^{-2}, an uneven surface with irregular protrusions appeared in the $Zn(BF_4)_2/H_2O$ electrolyte system only after electrodepositing 20 min. As the deposition time was prolonged, the protrusions gradually induced a self-amplification behavior, forming Zn dendrites, which may puncture the separator in the subsequent cycling process, leading to internal short circuits of ZIBs. In sharp contrast, Zn deposition behavior in the ZFT electrolyte system had been greatly improved. The Zn electrode maintained a dense and uniform deposition morphology without any dendrites as Zn deposition time throughout 40 min.

Besides, 2D-GIWAXS, and XRD were used to evaluate the crystal structure of the Zn deposition layer. As shown in Figure 4f, the 2D-GIWAXS pattern of Zn metal cycled in the $Zn(BF_4)_2/H_2O$ electrolyte system displayed multiple Debye rings, corresponding its disordered crystal structure. However, the diffraction intensity of Debye rings changed significantly when using the ZFT electrolyte and without the presence of heterocycles, where the (002) crystal plane had the highest diffraction intensity, proving the trend of Zn epitaxial deposition along the (002) crystal plane. The X-ray diffraction polarographic test also showed similar results. The (002) pole of Zn metal in ZFT electrolyte system exhibited a significant intensity concentration compared to that in ZFH electrolyte system, while the (101) pole of Zn metal cycled in ZFH electrolyte system had a very high intensity concentration, confirming the irregular random growth orientation (Figure S18, Supporting Information). Furthermore, the XRD patterns of Zn metal anode after different cycles can also confirm this conclusion. As shown in Figure 4g and Figure S19 (Supporting Information), there was a strong (002) crystal plane in the initial cycling stage in the ZFT electrolyte system, and the intensity ratio of Zn

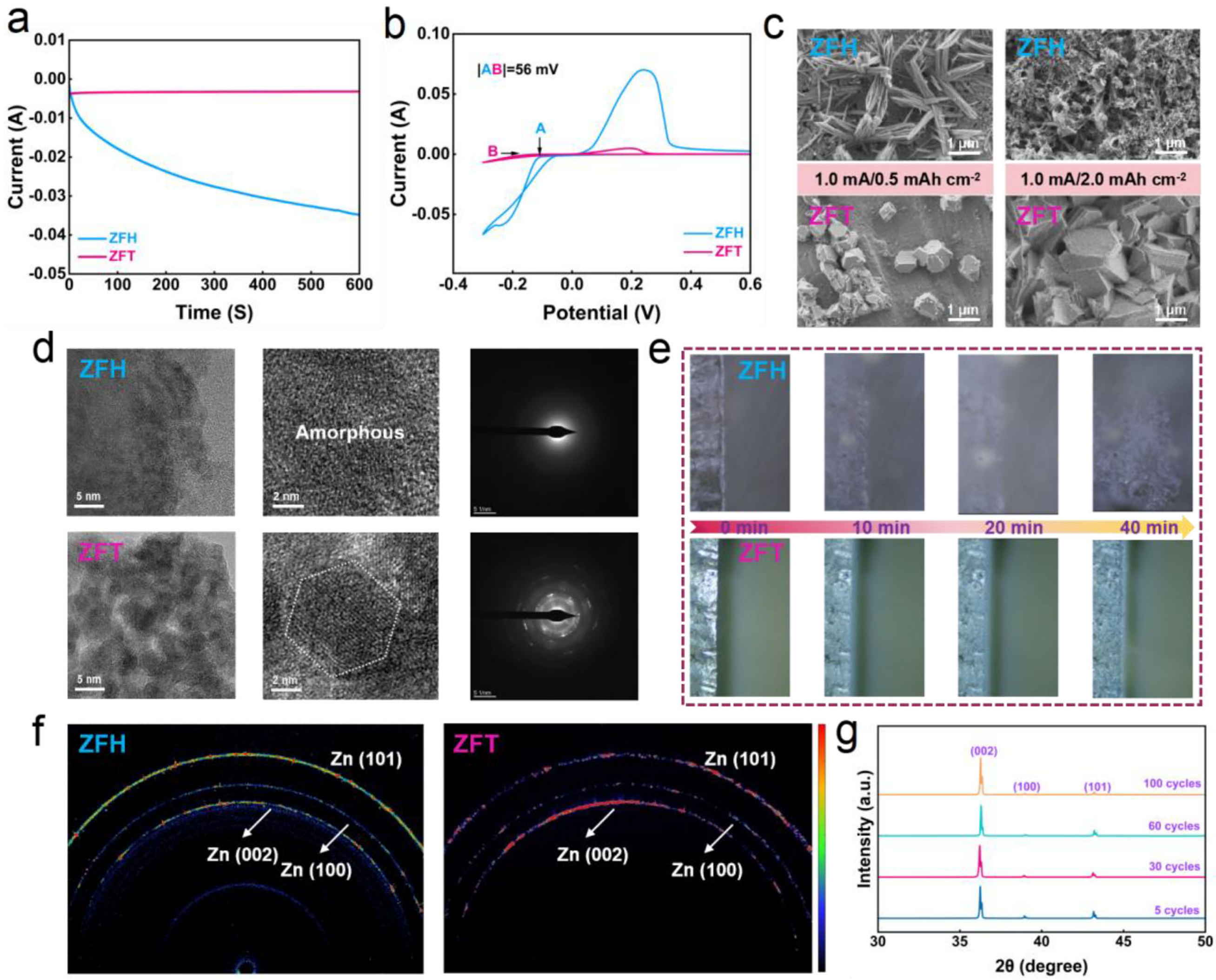

Figure 4. Nucleation and growth behavior of Zn^{2+} in borate-furan electrolyte. a) The i-t curves of Zn electrode in ZFH/ZFT at −150 mV; b) CV curves of SS|Zn half cells in ZFH/ZFT; c) Morphology of Zn deposition at different deposition capacities in ZFH/ZFT, the fixed current density was 1.0 mA cm^{-2}; d) HRTEM images of Zn deposited in ZFH/ZFT; e) In situ optical images of the Zn plating in ZFH/ZFT; f) The 2D GIWAXS results of the Zn deposition in ZFH/ZFT; g) XRD patterns of ZFT after different cycles.

(002) and Zn (101) crystal planes was 4.65 after 5 cycles. Meantime, the intensity ratio increased in the subsequent cycles (14.45 after 100 cycles), confirming that the preferential Zn growth toward (002) crystal plane can be promoted in the ZFT electrolyte system.

2.4. Electrochemical Performance and Cycling Stability

To investigate the reversibility of Zn metal anode in borate-furan electrolyte, Zn | Cu half cells and Zn || Zn symmetrical cells were assembled with thin Zn foils (30 μm). As shown in Figure S20 (Supporting Information), for the $Zn(BF_4)_2/H_2O$ electrolyte system, the coulombic efficiency (CE) of Zn | Cu half cells rapidly decreased to <80% after 40 cycles because of the severe interfacial side reactions and dendritic growth. In contrast, the cells can run stably in the ZFT electrolyte system for 800 and 750 cycles with high CE of 99.46% and 99.75% at the current densities of 0.5 and 1.0 mA cm^{-2}, respectively (Figure S20a,b, Supporting Information). Capacity-voltage curves can also confirm the enhanced reversibility of Zn plating/stripping behavior (Figure S20c,d, Supporting Information). When the current density was increased to 5.0 mA cm^{-2}, the cells can still stably run for >2400 cycles with a high CE of 99.81%, while the cells in the $Zn(BF_4)_2/H_2O$ electrolyte system can hardly work (**Figure** 5a). Meanwhile, we also evaluated the loss of active Zn during the cycling process using the average CE method, which was shown in Figure S21 (Supporting Information). In the ZFT electrolyte system, the average CE of was as high as 99.2%, proving that even in the initial stage, Zn metal can also deposit/strip more stably, reducing the loss of active Zn and improving cycling stability.[41]

The Zn || Zn symmetrical cells were also assembled to investigate the Zn plating/stripping reversibility in borate-furan electrolyte. As shown in Figure S22 (Supporting Information),

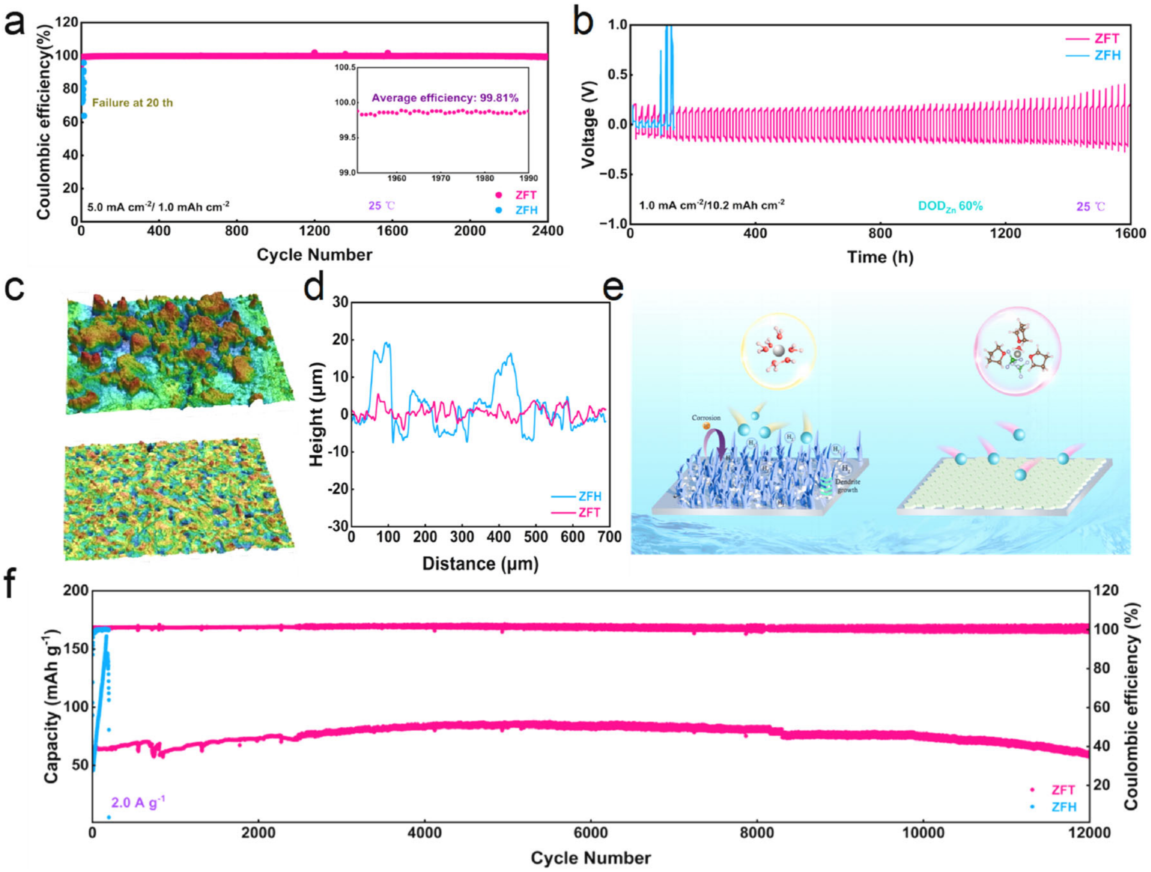

Figure 5. Electrochemical performance and cycling stability. a) Cycling performance of Zn | Cu half-cells in ZFH/ZFT electrolytes at 5.0 mA cm^{-2}/1.0 mAh cm^{-2}; b) The cycling performance of symmetrical Zn || Zn cells in ZFH/ZFT electrolytes electrolyte at 60%DOD; c,d) LSCM images and height fluctuation measurement of Zn deposited in ZFH/ZFT; e) Schematic diagrams of the Zn deposition behavior in the ZFH/ZFT electrolytes; f) Cycling performance of Zn||V_2O_5 full cell at the current density of 2.0 A g^{-1}.

at the current density of 1.0 mA cm^{-2}, the symmetrical cells can run stably >1400 h, far exceeding that in the $Zn(BF_4)_2/H_2O$ electrolyte system. Simultaneously, the cycling life of symmetric cells was compared under different salt concentrations, with the 0.45 м ZFT electrolyte exhibiting the most stable electrochemical performance (Figure S23, Supporting Information). More noteworthy is that even at a high area capacity of 10.2 mAh cm^{-2} (DOD = 60%), symmetrical cells can still achieve stable Zn plating/stripping behavior for over 1600 h, effectively improving the utilization rate of Zn metal anode (Figure 5b). In terms of rate performance, the symmetric cells demonstrated a smaller overpotential and stable cycling over 330 h (Figure S24, Supporting Information). These results strongly confirm that the ZFT electrolyte system can improve the electrochemical stability of Zn metal anode, meeting the practical requirements for high capacity, high current density, and long cycle life. Furthermore, the surface morphology of Zn electrodes after cycling was also investigated. As shown in Figure S25 (Supporting Information), for the Zn electrode cycled in the $Zn(BF_4)_2/H_2O$ electrolyte system, the electrode surface was severely corroded, quite rough, and uneven. However, the Zn electrode cycled in the borate-furan electrolyte maintained a very regular and dense surface even after 100 cycles, without the obvious by-products and dendrites. Similarly, the testing of LSCM was consistent with the above results. The Zn metal anode using ZFT electrolyte had a smooth and dense surface dominated by the Zn (002) crystal plane during deposition, while in the $Zn(BF_4)_2/H_2O$ electrolyte system, uneven surface with anisotropic dendrites can be clearly observed (Figure 5c,d; Figure S26, Supporting Information). Thus, we concluded the main Zn^{2+} nucleation and deposition mechanism, that is, the highly hybrid SEI layer derived from the unique inverse solvation configuration changed the Zn^{2+} deposition behavior, resulting in Zn growth along the Zn (002) crystal plane. At the same time, owing to the lower surface energy of Zn (002) crystal plane, its electrochemical activity for hydrogen evolution and corrosion response was suppressed, avoiding the formation of Zn dendrites and reducing parasitic reactions, thereby effectively improving the cycling stability of Zn metal anode (Figure 5e).

Further in order to explore the practical application prospect of the borate-furan electrolyte, we assembled the Zn || V_2O_5 and Zn||$NH_4V_4O_{10}$ full cells. Initial CV test results indicated that the ZFT electrolyte exhibited stable redox reactions, whereas the ZFH electrolyte lacked stable redox capability due to severe electrode corrosion (Figure S27, Supporting Information). Further long-cycle testing was conducted on the battery, at the current density of 2.0 A g^{-1}, the ZFT full cells can run over 12 000 cycles with a high CE of ≈100%, demonstrating ultra-long cycling stability, the corresponding charge-discharge curves also demonstrate stable cycling performance, whereas it can only be maintained for 100 cycles for ZFH electrolyte (Figure 5f; Figure S28, Supporting Information). Simultaneously, Zn||$NH_4V_4O_{1n}$ batteries were assembled to evaluate the suitability of the ZFT electrolyte. The results of the CV tests were consistent with those of V_2O_5, demonstrating the ZFT electrolyte's stable redox capability (Figure S29, Supporting Information). Furthermore, the rate testing results indicated its excellent rate capability (Figure S30, Supporting Information). Subsequently, we employed $NH_4V_4O_{10}$ with a higher loading (>6 mg cm^{-2}, N/P ratio: ≈10) as the cathode to assemble a Zn||$NH_4V_4O_{10}$ battery, as shown in Figure S31 (Supporting Information). At a current density of 2.0 A g^{-1}, the Zn||$NH_4V_4O_{10}$ full cell demonstrated stable cycling performance exceeding 1000 cycles with negligible capacity decay, confirming its practical application potential.

2.5. Electrochemical Performance of Batteries under Harsh Conditions

In order to validate the applicability of ZFT electrolytes in ZIBs, we evaluated the applicability of the borate-furan electrolyte under harsh conditions. First, the tolerance to low temperatures was analyzed, and such an electrolyte can maintain good fluidity even at −40 °C (Figure S32, Supporting Information). The DSC curves further substantiated that the borate-furan electrolyte did not undergo phase transition at the temperatures as low as −100 °C, with a freezing point as low as −120.9°C, highlighting its excellent low-temperature tolerance (Figure S33, Supporting Information).

In terms of electrochemical performance, since the ZFH electrolyte freezes at low temperatures, its electrochemical properties are not compared, at −20 °C, the Zn || Zn symmetrical cells can run stably over 7000 h at the current density of 0.5 mA cm^{-2} for ZFT electrolyte, with ultra-long cycling capability (**Figure 6**a). Besides, we also evaluated the plating/stripping reversibility of Zn metal anode at high discharge depths at −20 °C, which was shown in Figure 6b. At a fixed capacity of 10.2 mA h cm^{-2} (DOD = 60%), symmetric batteries exhibited a highly stable voltage curve within 3500 h, demonstrating strong competitiveness compared to previously reported batteries and showing practical prospects under harsh conditions (Figure 6c).[26,27,42–54] Considering the integrity of the electrode SEI at high depth of discharge (DOD), we performed XPS characterization with varying sputtering durations on cycled electrode sheets at −20 °C under high DOD conditions. As shown in Figure S34 (Supporting Information), the SEI layer remained highly stable at low temperatures and high DOD, with inorganic components such as ZnF_2 and ZnO still dominating. This ensured rapid Zn^{2+} conduction kinetics at low temperatures and high DOD, thereby delivering outstanding cycling performance. Further, even at −40 °C, the Zn || Zn symmetrical cells can work for over 3500 h at the current densities of 0.25 mA cm^{-2} (Figure S35, Supporting Information). Correspondingly, we also investigated the cycling stability of Zn | Cu half cells at low temperatures. As shown in Figure S36 (Supporting Information), the cells can be cycled over 2200 cycles at −20 °C with a high average CE of 99.15%. When the temperature is further reduced to −40 °C, Zn | Cu half cells can still be stably run >2000 cycles with a high average CE of 99.55%, showing great low-temperature adaptability (Figure 6d). Next, when the borate-furan electrolyte was matched with the PANI cathode, at low temperatures, the full cells can run >18 000 cycles at a current density of 0.5 A g^{-1} with a high CE of ≈100% (Figure 6e). Compared to previously reported advanced low-temperature electrolytes, the ZFT electrolyte demonstrated significant advantages and showed promising practical application prospects (Figure S37, Supporting Information). Meanwhile, the pouch cells assembled with such a borate-furan electrolyte can activate the light plate connected by LED small lights, reflecting its practical prospects (Figure 6f).

In addition, we explored the mechanism underlying the differences in electrochemical performance of the borate-furan electrolyte at different temperatures. First, the ionic conductivities of ZFT electrolytes at different temperatures were compared. Because the inverse solvation configuration sheath layer of ZFT is mainly dominated by small-molecule organic solvents and anions, with minimal participation of water molecules, the solvation structure remains largely unaffected by temperature variations, which ensures the desolvation ability of zinc ions at low temperature. Therefore, the ZFT electrolytes still exhibited a high ionic conductivity of 13.3 mS cm^{-1} even at ultra-low temperatures of −40 °C, which can effectively maintain the run of ZIBs (Figure S38, Supporting Information). The LSV and Tafel curves showed that the hydrogen bonding network of free water molecules was disrupted under low temperatures, and there were almost no hydrogen evolution or corrosion reactions, improving the interface stability of Zn metal anode (Figure S39, Supporting Information). So that the Zn deposition demonstrated a more uniform morphology at low temperatures (Figure S40, Supporting Information). Furthermore, we also simulated the surface state of Zn metal at different temperatures. As shown in Figure 6g and Figure S41 (Supporting Information), the Zn surface had a more uniform electric field distribution, ion concentration distribution, and current density distribution at low temperatures, inducing Zn^{2+} to maintain a relatively uniform morphology throughout the entire deposition process. Besides, we evaluated the application of the borate-furan electrolyte at high temperatures. As shown in Figure S42 (Supporting Information), at 40 °C, the Zn metal anode can run over 800 h in symmetrical cells and >400 cycles with a high CE of 99.64% in half cells, showing high stability.

In short, compared with the common ZIBs electrolyte, the extremely simplified borate-furan electrolyte exhibited significant tolerance to harsh environments, the cells can cycle stably over a wide temperature range (−40 to 40 °C), highlighting the broad application prospects (Figure 6h).

3. Conclusion

In summary, we reported an extremely simplified low-concentration inverse solvation configuration electrolyte (0.45 M) composed of hydrated $Zn(BF_4)_2$ and tetrahydrofuran, achieving a highly reversible Zn metal anode with high Zn utilization. The results of theoretical analysis and experimental study show that tetrahydrofuran reshapes the Zn^{2+} solvation structure through a spatial confinement effect, effectively reversing the conventional active-water-dominated solvation environment

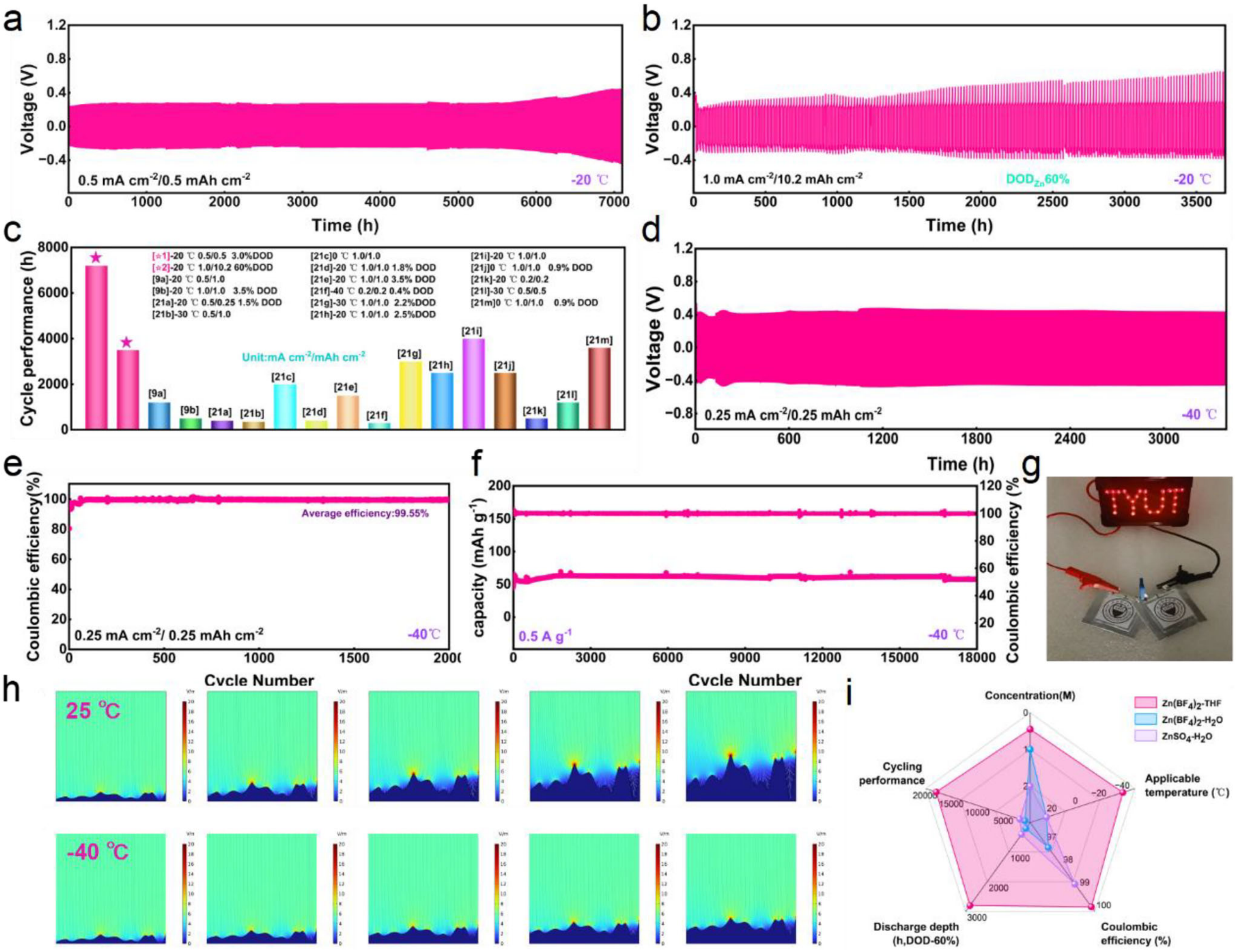

Figure 6. Electrochemical performance and cycling stability. a) Cycling performance of Zn || Zn symmetric cells at 0.5 mA cm^{-2}/0.5 mAh cm^{-2} under −20 °C; b) DOD testing of symmetrical cells at −20 °C; c) Comparison of the Zn anodes in ZFT electrolyte with recently reported Zn anodes at low temperatures; d) The cycling performance of Cu | Zn half cells under −40 °C; e) Long-term cycling stability of Zn||PANI cells at a current density of 0.5 A g^{-1} in −40 °C; f) Practical application demonstration; g) Electric field distribution during simulated zinc deposition at different temperatures; h) Overall advantages of ZFT electrolytes.

($[Zn(H_2O)_6]^{2+}$) typical of aqueous electrolytes. This reorganization leads to a distinctive inverse solvation configuration ($[Zn(THF)_3(H_2O)]^{2+}\cdot(BF_4^-)_2$) dominated by small organic solvent molecules. Consequently, this structure not only accelerates the desolvation kinetics but also facilitates the formation of a favorable organic–inorganic hybrid SEI layer to control the deposition behavior of Zn to promote the formation of a dendrite-free Zn deposition state with a high degree of (002) texture, thus obtaining excellent interface stability. Therefore, the obtained battery showed excellent electrochemical performance, the Zn | Cu half cells can be cycled for 2400 cycles at a high Coulombic efficiency of 99.81% at 25 °C, the symmetric Zn || Zn cells can run at a low temperature of −20 °C for >7000 h, the Zn || PANI full batteries did not show significant capacity degradation even after 18 000 cycles, more prominently, even at a high discharge depth of 60%, the Zn || Zn symmetrical cells still can cycle 3500 h at low temperature, highlighting the broad application prospects. This work is expected to inspire more sustainable ZIBs work in developing low-cost, high-performance, industrialized production.

Supporting Information

Supporting Information is available from the Wiley Online Library or from the author.

Acknowledgements

This work was supported by the National Natural Science Foundation of China (52071227, 22572140, U24A6002, U25A20628, 22561160129, 22479074, 22475096), the Beijing Natural Science Foundation-Xiaomi innovation joint Foundation (L223011), Young Elite Scientists Sponsorship Program by CAST(2022QNRC001), Fundamental Research Program of Shanxi Province (202103021222006), Shanxi energy internet research institute (SXEI2023A004), International Science and Technology Cooperation and Exchange Special Project in Shanxi Province (202104041101016), Key Scientific Research Project in Shanxi Province (202102050201003), the special fund for Science and Technology Innovation Teams of Shanxi Province(202204051001004), the Equipment Pre-Research and Ministry of Education Joint Fund (8091B02052407), the Fundamental Research Program Key Project of Jiangsu Province (BK20253008), the Science and Technology Major Project of Jiangsu Province (BG2024013), the Scientific and Technological Achievements Transformation Special Fund of Jiangsu Province (BA2023037), the Academic Degree and Postgraduate Education Reforming Project of Jiangsu Province (JGKT24_C001), the Key Core Technology Open Competition Project of Suzhou City (SYG2024122), the Open Research Fund of Suzhou Laboratory (SZLAB-1308-2024-TS005), and the Chenzhou National Sustainable Development Agenda Innovation Demonstration Zone Provincial Special Project (2023sfq11). The authors would like to thank Zhenyu Duan from Shiyanjia Lab (www.shiyanjia.com) for the HRTEM and TOF-SIMS analysis.

Conflict of Interest

The authors declare no conflict of interest.

Data Availability Statement

The data that support the findings of this study are available from the corresponding author upon reasonable request.

Keywords

high discharge depth, inverse solvation configuration, low concentration, ultralong cycle life, Zn metal anode

Received: September 3, 2025
Revised: November 12, 2025
Published online:

[1] D. Kundu, B. D. Adams, V. Duffort, S. H. Vajargah, L. F. Nazar, *Nat. Energy* **2016**, *1*, 119.
[2] G. Fang, J. Zhou, A. Pan, S. Liang, *ACS Energy Lett.* **2018**, *3*, 2480.
[3] Q. Wang, T. Lu, Y. Liu, J. Dai, L. Guan, L. Hou, H. Du, H. Wei, X. Liu, X. Han, Z. Ye, D. Zhang, Y. Wei, H. Zhou, *Energy Storage Mater.* **2023**, *55*, 782.
[4] T. Lu, Y. Lin, L. Guan, L. Hou, H. Du, H. Wei, X. Liu, C. Yang, Y. Wei, M. Song, W. Liu, H. Zhou, Q. Wang, *ACS Appl. Energy Mater.* **2023**, *7*, 61.
[5] Y. Li, L. Wang, Z. Sun, D. Li, Z. Yuan, H. Liu, G. Li, J. Li, W. Han, *Adv. Mater.* **2025**, *37*, 08336
[6] T. Zhang, Y. Tang, S. Guo, X. Cao, A. Pan, G. Fang, J. Zhou, S. Liang, *Energy Environ. Sci.* **2020**, *13*, 4625.
[7] S. W. D. Gourley, R. Brown, B. D. Adams, D. Higgins, *Joule* **2023**, *7*, 1415.
[8] Y. Li, Z. Yuan, D. Li, J. Li, Y. Zhang, M. Wang, G. Li, L. Wang, W. Han, *ACS Nano* **2024**, *18*, 4733.
[9] F. Wang, O. Borodin, T. Gao, X. Fan, W. Sun, F. Han, A. Faraone, J. A. Dura, K. Xu, C. Wang, *Nat. Mater.* **2018**, *17*, 543.
[10] S. Chen, D. Ji, Q. Chen, J. Ma, S. Hou, J. Zhang, *Nat. Commun.* **2023**, *14*, 3526.
[11] C. Nie, G. Wang, D. Wang, M. Wang, X. Gao, Z. Bai, N. Wang, J. Yang, Z. Xing, S. Dou, *Adv. Energy Mater.* **2023**, *13*, 2300606.
[12] X. Yu, Z. Li, X. Wu, H. Zhang, Q. Zhao, H. Liang, H. Wang, D. Chao, F. Wang, Y. Qiao, H. Zhou, S.-G. Sun, *Joule* **2023**, *7*, 1145.
[13] N. Hu, W. Lv, W. Chen, H. Tang, X. Zhang, H. Qin, D. Huang, J. Zhu, Z. Chen, J. Xu, H. He, *Adv. Funct. Mater.* **2023**, *34*, 2311773.
[14] R. Zhang, W. K. Pang, J. Vongsvivut, J. A. Yuwono, G. Li, Y. Lyu, Y. Fan, Y. Zhao, S. Zhang, J. Mao, Q. Cai, S. Liu, Z. Guo, *Energy Environ. Sci.* **2024**, *17*, 4569.
[15] D. Xie, H.-H. Liu, C. Liu, W.-Y. Diao, F.-Y. Tao, W.-B. Jiang, H.-Z. Sun, J.-W. Wang, H. Yu, W.-L. Li, X.-L. Wu, J.-P. Zhang, *Energy Storage Mater.* **2024**, *70*, 103524.
[16] N. Chang, T. Li, R. Li, S. Wang, Y. Yin, H. Zhang, X. Li, *Energy Environ. Sci.* **2020**, *13*, 3527.
[17] K. Guan, W. Chen, Y. Yang, F. Ye, Y. Hong, J. Zhang, Q. Gu, Y. Wu, L. Hu, *Adv. Mater.* **2024**, *36*, 2405889.
[18] C. You, R. Wu, X. Yuan, L. Liu, J. Ye, L. Fu, P. Han, Y. Wu, *Energy Environ. Sci.* **2023**, *16*, 5096.
[19] N. Patil, C. de la Cruz, D. Ciurduc, A. Mavrandonakis, J. Palma, R. Marcilla, *Adv. Energy Mater.* **2021**, *11*, 2100939.
[20] S. You, Q. Deng, Z. Wang, Y. Chu, Y. Xu, J. Lu, C. Yang, *Adv. Mater.* **2024**, *36*, 2402245.
[21] J. Wan, R. Wang, Z. Liu, S. Zhang, J. Hao, J. Mao, H. Li, D. Chao, L. Zhang, C. Zhang, *Adv. Mater.* **2023**, *36*, 2310623.
[22] W. He, Y. Ren, B. S. Lamsal, J. Pokharel, K. Zhang, P. Kharel, J. J. Wu, X. Xian, Y. Cao, Y. Zhou, *ACS Appl. Mater. Interfaces* **2023**, *15*, 6647.
[23] D. Wang, H. Peng, S. Zhang, H. Liu, N. Wang, J. Yang, *Angew. Chem., Int. Ed.* **2023**, *62*, 202315834.
[24] J. Qiang, W. Yu, Y. Zhao, L. Zhang, Y. Chen, Z. Gao, Y. An, S. Le, Y. Mao, G. Zhao, *Electrochim. Acta* **2024**, *481*, 143929.
[25] Q. Zhang, Y. Ma, Y. Lu, L. Li, F. Wan, K. Zhang, J. Chen, *Nat. Commun.* **2020**, *11*, 4463.
[26] D. Feng, F. Cao, L. Hou, T. Li, Y. Jiao, P. Wu, *Small* **2021**, *17*, 2103195.
[27] K. Qiu, G. Ma, Y. Wang, M. Liu, M. Zhang, X. Li, X. Qu, W. Yuan, X. Nie, N. Zhang, *Adv. Funct. Mater.* **2024**, *34*, 2313358.
[28] Y. Dong, N. Zhang, Z. Wang, J. Li, Y. Ni, H. Hu, F. Cheng, *J. Energy Chem.* **2023**, *83*, 324.
[29] X. Lin, G. Zhou, M. J. Robson, J. Yu, S. C. T. Kwok, F. Ciucci, *Adv. Funct. Mater.* **2021**, *32*, 2109322.
[30] X. Li, M. Wang, Y. Chu, Y. Gao, Z. Yang, Y. Feng, J. Chen, Z. Ma, B. Guo, B. Yu, Y. Huang, X. Li, *Chem. Eng. J.* **2024**, *487*, 150588.
[31] S. Wang, Y. Ying, S. Chen, H. Wang, K. K. K. Cheung, C. Peng, H. Huang, L. Ma, J. A. Zapien, *Energy Storage Mater.* **2023**, *63*, 102971.
[32] P. Cui, T. Wang, Z. Wang, H. Geng, P. Song, F. Hu, J. You, K. Zhu, *Chem. Eng. J.* **2024**, *500*, 156971.
[33] G. Ma, S. Di, Y. Wang, W. Yuan, X. Ji, K. Qiu, M. Liu, X. Nie, N. Zhang, *Energy Storage Mater.* **2023**, *54*, 276.
[34] R. He, F. Yu, K. Wu, H.-X. Liu, Z. Li, H. K. Liu, S.-X. Dou, C. Wu, *Nano Lett.* **2023**, *23*, 6050.
[35] D. Han, C. Cui, K. Zhang, Z. Wang, J. Gao, Y. Guo, Z. Zhang, S. Wu, L. Yin, Z. Weng, F. Kang, Q.-H. Yang, *Nat. Sustain.* **2021**, *5*, 205.
[36] G. Ma, L. Miao, W. Yuan, K. Qiu, M. Liu, X. Nie, Y. Dong, N. Zhang, F. Cheng, *Chem. Sci.* **2022**, *13*, 11320.
[37] W. Yang, X. Du, J. Zhao, Z. Chen, J. Li, J. Xie, Y. Zhang, Z. Cui, Q. Kong, Z. Zhao, C. Wang, Q. Zhang, G. Cui, *Joule* **2020**, *4*, 1557.
[38] Y. Dong, L. Miao, G. Ma, S. Di, Y. Wang, L. Wang, J. Xu, N. Zhang, *Chem. Sci.* **2021**, *12*, 5843.
[39] X. Nie, L. Miao, W. Yuan, G. Ma, S. Di, Y. Wang, S. Shen, N. Zhang, *Adv. Funct. Mater.* **2022**, *32*, 2203905.
[40] X. Xu, Y. Chen, D. Zheng, P. Ruan, Y. Cai, X. Dai, X. Niu, C. Pei, W. Shi, W. Liu, F. Wu, Z. Pan, H. Li, X. Cao, *Small* **2021**, *17*, 2101901.
[41] B. D. Adams, J. Zheng, X. Ren, W. Xu, J. G. Zhang, *Adv. Energy Mater.* **2017**, *8*, 1702097.
[42] N. Wang, M. Sun, X. Ren, L. Hu, Z. Li, X. Yao, C. Jia, *Energy Storage Mater.* **2024**, *68*, 103333.
[43] S. Chen, J. Chen, X. Liao, Y. Li, W. Wang, R. Huang, T. Zhao, S. Yan, Z. Yan, F. Cheng, H. Wang, *ACS Energy Lett.* **2022**, *7*, 4028.
[44] Z. Hou, Z. Lu, Q. Chen, B. Zhang, *Energy Storage Mater.* **2021**, *42*, 517.

[45] Z. Wang, J. Diao, J. N. Burrow, Z. W. Brotherton, N. A. Lynd, G. Henkelman, C. B. Mullins, *Adv. Funct. Mater.* **2023**, *34*, 2311271.

[46] T. Sun, X. Yuan, K. Wang, S. Zheng, J. Shi, Q. Zhang, W. Cai, J. Liang, Z. Tao, *J. Mater. Chem. A* **2021**, *9*, 7042.

[47] H.-I. Kim, K. M. Lee, W.-Y. Kim, S. H. Kweon, X. Wang, S. Zheng, S.-H. Kim, J. H. Ha, S. J. Kang, Z.-S. Wu, S. K. Kwak, S.-Y. Lee, *Energy Environ. Sci.* **2024**, *17*, 1961.

[48] H. Du, X. Qi, L. Qie, Y. Huang, *Adv. Funct. Mater.* **2023**, *33*, 2302546.

[49] F.-D. Yu, Z.-J. Yi, R.-Y. Li, W.-H. Lin, J. Chen, X.-Y. Chen, Y.-M. Xie, J.-H. Wu, Z. Lan, L.-F. Que, B.-S. Liu, H. Luo, Z.-B. Wang, *J. Energy Chem.* **2024**, *91*, 245.

[50] W. Song, X. Xie, L. Deng, A. Pan, G. Cao, S. Liang, G. Fang, *Energy Storage Mater.* **2024**, *70*, 103489.

[51] H. He, H. Qin, F. Shen, N. Hu, J. Liu, *Chem. Commun.* **2021**, *57*, 11477.

[52] T. Wei, Y. Ren, Z. Li, X. Zhang, D. Ji, L. Hu, *Chem. Eng. J.* **2022**, *434*, 134646.

[53] S. Huang, L. Hou, T. Li, Y. Jiao, P. Wu, *Adv. Mater.* **2022**, *34*, 2110140.

[54] X. Cheng, Y. Zuo, Y. Zhang, X. Zhao, L. Jia, J. Zhang, X. Li, Z. Wu, J. Wang, H. Lin, *Adv. Sci.* **2024**, *11*, 2401629.